Muscle and intestine innexins with muscle Deg/Enac channels promote muscle coordination and embryo elongation

Running title (*max 32 characters*): understanding muscle coordination

Keywords (*3 to 6*): Morphogenesis, muscle activity, innexins, Deg/Enac channels, C. elegans

Flora LLENSE[1*], Teresa FERRARO[1], Xinyi YANG[#], Hanla SONG[$], & Michel LABOUESSE [1*]

1Sorbonne Université, IBPS, CNRS UMR7622, 7 Quai St-Bernard, 75005 Paris, France

[#] Present address: MRC-LMB, Francis Crick Ave, Trumpington, Cambridge CB2 0QH, UK

[$] Present address: Samsung Biologics, Yeonsu-gu, Incheon, 21987, KR

*Co corresponding authors: flora.llense@sorbonne-universite.fr and michel.labouesse@sorbonne-universite.fr

Abstract

Body axis elongation represents a fundamental morphogenetic process in development, which involves cell shape changes powered by mechanical forces. How mechanically interconnected tissues coordinate in organismal development remains largely unexplored. During *C. elegans* elongation, cyclic forces generated by muscle contractions induce remodeling of adherens junctions and the actin cytoskeleton in the epidermis, facilitating gradual embryo lengthening. While previous studies have identified key players in epidermal cells, understanding how muscle cells coordinate their activity for proper embryo elongation remains unsolved. Using a Calcium sensor to monitor muscle activity during elongation, we identified two cells in each muscle quadrant with a pacemaker-like function that orchestrate muscle activity within their respective quadrants. Strikingly, ablation of these cells halted muscle contractions and delayed elongation. A targeted RNAi screen focusing on communication channels identified two innexins and two Deg channels regulating muscle activity, which proved required for normal embryonic elongation. Interestingly, one innexin exhibits specific expression in intestinal cells. Our findings provide novel insights into how embryonic body wall muscles coordinate their activity and how interconnected tissues ensure proper morphogenesis.

Introduction

Tissue and embryo morphogenesis rely on intermingled cellular processes regulated by biochemical signalling pathways, and physical forces from surrounding cells and tissues (Zinner *et al.*, 2020). Most organs consist of multiple tissue layers that are mechanically coupled via the extracellular matrix (Nelson and Gleghorn, 2012; Mitchell *et al.*, 2022). Understanding how cell shape changes influence embryo-scale dynamics remains challenging. While some

molecular players in mechanical force transmission are known, coordination between mechanically coupled tissues for proper morphogenesis remains unclear.

C. elegans embryo elongation, which depends on cell shape changes driven by the epidermis, provides an ideal system to tackle these questions (Vuong-Brender *et al.*, 2016). It involves two phases: the first, from the comma to the 2-fold stages, depends on tension and stiffness anisotropy in the epidermis (Vuong-Brender *et al.*, 2017); beyond the 2-fold stage, it requires muscles, which are tightly attached to the epidermis through hemidesmosomes and a common extracellular matrix (Fig. 1A) (Vuong-Brender, *et al* 2016). Four body wall muscle quadrants are running along the anterior-posterior direction, two dorsal and two ventral (Gieseler *et al.*, 2017). Muscle contractions trigger a mechanotransduction pathway within the overlying epithelial layer. It activates PAK-1 (p21-activated kinase homologue) and subsequently remodels hemidesmosome components and the actin cytoskeleton (Zhang *et al.*, 2011; Lardennois *et al.*, 2019).

Whereas muscle cell dynamics in the adult and larval stages are well known (Gieseler *et al.*, 2017), little is known about embryonic muscle dynamics. In particular, we do not know how muscle cells initiate their contractions in embryos and how they coordinate their activity within each quadrant. The regulation of muscle contractions is unlikely to depend on synaptic input. Indeed, axonogenesis is still underway during the first embryonic contractions (Wu *et al.*, 2011; Shah *et al.*, 2017; Moyle *et al.*, 2021). Moreover, mutants defective for acetylcholine or GABA release such as *unc-17* or *snb-1*, which cause complete paralysis in larvae, do not trigger the Paralyzed at two-fold (Pat) typical of mutants affecting myofilament attachment (such as *pat-2/3* or *unc-112*) (Alfonso *et al.*, 1993; Nonet *et al.*, 1998)

Here, to improve our understanding of muscle coordination in elongating embryos, we explored muscle activity by calcium imaging. To identify new molecular players involved in regulating muscle activity, we performed a RNAi

screen targeting innexins (Simonsen *et al.*, 2014), which are gap junction components, and degenerin/epithelial sodium channels (Deg/Enac channels) (Geffeney *et al.*, 2011; Eastwood and Goodman, 2012). Remarkably, we establish that two innexins and two Deg/Enac channels play a crucial role in coordinating muscle contractions within a quadrant to ensure a dynamic and progressive lengthening of the embryo. Our work thus further explains how muscles and the epidermis jointly drive embryonic morphogenesis.

Results and discussion

Embryonic body muscles organization and dynamics

We aimed to investigate how muscle activity is initiated and controlled during elongation (Fig. 1A). To track muscle activity over time, we used the ratiometric GCaMP calcium sensor expressed under the muscle-specific *myo-3* promotor (Schwarz, *et al.*, 2012). A time-lapse analysis was conducted to examine the variation of probe intensity in two lateral muscle quadrants within the field of view Fig. 1B; Movie 1). We found in wild-type embryos that the GCaMP signal first showed up in five adjacent cells in each quadrant, and that dorsal and ventral quadrant are not synchronized. We called them cell-1 to cell-5 according to their positions along the anterior-posterior axis (Fig. 1C). Cell-2 and cell-3 were located just posterior to pharyngeal PHA-4 positive cells, and cell-4 was at the level of the V1 lateral epidermal cell (Fig. S1A et B). We conclude that the identity of left cell-2 and cell-3, which play a key role (see below), are dorsally MSappap (cell-2d) and Daaap (cell-3d); and ventrally Daaaa (cell-2v) and Dapaa (cell-3v).

We analyzed the calcium signal in each quadrant and compiled the intensity profiles. We observed that the intensity and duration of each calcium pulse correlated with a contraction of the corresponding muscle cell (Fig. 1D). Hence, GCaMP signals represent a good proxy for muscle contractions in the embryo. We subsequently extracted several parameters such as the duration of the calcium pulses (Fig. 1E), the delay between pulses among adjacent cells,

(Fig. 1F), and their intensity (Fig. 1G). We noticed that muscle contractions originated in dorsal quadrants (Movie1), and that each pulse lasted roughly 6 seconds in cells-1/5 (Fig. 1E). The intensity of contractions differed among cells, with the highest intensity observed in cell-2 and cell-3 (Fig. 1F), which always pulsed first in a given quadrant. Subsequently, the calcium activity shifted to muscle cells-1/4/5, leading us to hypothesize that cell-2 and cell-3 may act as pacemaker cells (Fig. 1E-G). Plotting the intensity versus the delay in pulsing confirmed the existence of two populations within each muscle quadrant, cell-2 and cell-3 (red dots in Fig. 1H) versus the other cells (blue dots in Fig. 1H).

To further investigate the dynamics of contractions between muscle quadrants during elongation, we examined whether they were connected. Using a muscle membrane marker, we conducted long time-lapse movies starting at the 1.2-fold stage (Movie 2; Fig. S1C). We confirmed that muscle quadrants are connected by long membrane extensions (Viveiros *et al.*,2011). We observed that the two dorsal muscle quadrants as well as the dorsal and ventral quadrants were connected by one (68% of embryos) or more extensions (32% of embryos) involving cell-1 to cell-5 (Fig. S1D). However, in the 22 examined embryos, the two ventral quadrants had only exceptionally a connection (Fig. S1D). Importantly, these connections were not formed de novo, but rather were residual connections occurring as the muscle cells migrate to reach their final location (Movie 2), and generally disappeared shortly after the 2-fold stage. It is tempting to speculate that these connections account for the early coordination between muscle quadrants, even if we could not prove it. In conclusion, our data reveal the existence of five cells initiating the wave of muscle contractions.

Cell-2 and cell-3 mimic the role of a pacemaker

To clarify the role of cell-2 and cell-3, we ablated these cells by expressing a miniSOG construct (Xu and Chisholm, 2016), which induces photo-damage through the formation of active oxygen species when illuminated at 458 nm. Expressing the miniSOG construct only in muscle cells, we specifically photo-

ablated cell-2 and cell-3 together in dorsal and ventral left quadrants before muscle contractions started, and analyzed if muscle contraction was impaired or not. As controls, we also photo-ablated three areas of similar size located either in head muscles, tail muscles or head neurons. We observed that targeted ablation of cell-2 and cell-3 resulted in slower elongation by impairing muscle contractions and embryo rotations (Fig. 2A, E-F and Movie 3). When similar ablations were made in control areas, muscle activity remained normal (Fig. 2D). To quantify this behavior, we examined the intensity profile along a line passing through cell-2 and cell-3 in both quadrants, reasoning that if muscles could still contract, a signal along this line should be visible in a kymograph (Fig. 2B, C-D). By comparing the intensity profile between control embryos without ablation, we identified a decrease in intensity only when cell-2 and cell-3 were ablated (Fig. 2D). This result confirms that cell-2 and cell-3 initiate the calcium wave and suggests that they act as pacemaker during muscle quadrant contraction.

Two innexins coordinate muscle activity

To determine how muscle contractions are controlled and are coordinated among the four quadrants, we performed a gene candidate RNAi screen. We focused on three gene families: the innexins, the DEG/ENAC channels some of which are mechanoresponsive ion channels, and TRP channels expressed in embryos. In total, we tested 47 candidate genes (Table S1). From this screen, we identified two innexins leading to a defect in muscle activity, INX-18 and INX-15. We confirmed their role using the strong mutant *inx-18(ok2454)* (Voelker *et al.*, 2019) and a newly CRISPR-induced mutant *inx-15(syb5414)* deleting the first two transmembrane domains.

We confirmed that INX-18 is expressed in muscle cells by using a GFP translational (Fig. 3A) and transcriptional reporter constructs (Fig. S2D) (Liu *et al.*, 2013). In *inx-18* knockdown and *inx-18(ok2454)* embryos, we observed a ventral bump with more constricted muscle cells (Fig. S2A-B). We further

observed that cell-2 and cell-3 were now pulsing at the same time as cells-1/-4/5 (Fig. 3B) and with a lower calcium intensity, suggesting that the latter might have lost their pacemaker-like role (Fig. 3C, I). However, in *inx-18(ok2454)* mutants, the duration of the contraction (Fig. 3D), the frequency of contractions and the speed of the calcium wave were unchanged compared to wild-type embryos (Fig.S1E-F). Since muscles are important for elongation, we next examined if elongation was perturbed in the absence of INX-18 (Fig. 3J). We found that the muscle-dependent phase of elongation was slower, and that the final length of the embryo was shorter than in wild-type embryos. Intriguingly, the *inx-18* mutant elongation curve resembles that of a *pak-1* mutant (Lardennois *et al.*, 2019), raising the possibility that proper coordination of muscle contraction stimulates PAK-1 activity (Fig. 3J).

Interestingly, INX-15 was only expressed in intestinal cells, as previously reported(Altun ZF *et al.*,2009), showing a continuous distribution between intestinal cells and a punctate one basally (Fig. 3E). Analysis of the calcium profile in *inx-15(RNAi)* and *inx-15(syb5414)* embryos revealed, as in *inx-18* mutants, that cell-2 and cell-3 were now pulsing at the same time as cells-1/4/5 with a lower GCaMP intensity (Fig. 3F, G, H). Likewise, we observed that *inx-15(syb5414)* embryos elongated more slowly and that hatching larvae were shorter than wild-type larvae (Fig. 3J-K). Additionally, the duration of the contraction in *inx-15(RNAi)* was shorter, although it did not affect elongation speed (Fig. 3J). Importantly, expressing an INX-15::mCherry construct under the intestine-specific promoter *elt-2* rescued the length of *inx-15(syb5414)* hatching larvae (Fig. 3K). Hence, intestinal cells participate in the maintenance of muscle cell activity, much like they also coordinate muscle activity during defecation (Peters *et al.*, 2007).

Since *inx-15* and *inx-18* mutants lead to similar phenotypes, we examined their interactions by constructing an *inx-15; inx-18* double mutant and analyzing their phenotype. We found that the size of double mutant hatching L1 larvae was similar to that of *inx-15* and *inx-18* single mutants (Fig. 3J), suggesting that they

are acting in the same pathway Likewise, the calcium profile of double mutants was statistically similar (Fig. S2E-F), although there was a slight but significant difference between the double and inx-15 single mutant (Table S2). Altogether these results highlight a new role of the innexin family in muscle activity controls and reveal that the intestine is also required for normal embryonic elongation.

Two Deg/Enac channels coordinate muscle activity

Although we did not identify any DEG/ENAC channel leading to a muscle phenotype in RNAi screen, the further analysis of two gain of function mutants, *deg-1(u506)* and *unc-105(n506)* (Park and Horvitz, 1986; Liu, *et al.*,1996; Takagaki *et al.*, 2020), uncovered their role in regulating muscle contractions.

Calcium profile analysis of *deg-1(u506)* showed that cell-1/cell-5 contracted uncoordinatedly and randomly (Fig. 4A). We also observed that their contractions lasted around 2 s instead of 6 s in controls (Fig. 4B-D). This suggest that the pacemaker-like activity of cell-2 and cell-3 was abolished, leading to an aberrant contraction pattern and unproductive contractions. Furthermore, we confirmed that *deg-1(u506)* embryos arrest at the 2-fold stage at 16°C (Fig. 4E)(García-Añoveros *et al.*, 1995). To further characterize the role of DEG-1, we analyzed its localization by looking at the expression of a DEG-1::GFP knockin. We observed a sparse dotty pattern of the DEG-1::GFP marker in the embryo (Fig. 4G). Colocalizing DEG-1::GFP with three additional markers, showed that muscle cells expressed it, in the same focal plane as EMB-9/Collagen IV (Fig. 4G; Fig. S3A). We conclude that normal DEG-1 activity is required to coordinate muscle contractions and to ensure normal pacemaker activity, both of which are essential for normal elongation.

We found that the *unc-105(n506)* gain-of-function mutation resulted in embryos with normal contraction time and delay in pulsing (Fig. 4A-D).). However, a higher calcium intensity profile was observed in cell-2 and cell-3 compared to wild-type embryos (Fig. 4B, D). Furthermore, we observed that embryonic elongation was affected resulting in shorter terminal embryos than controls (Fig.

4F), presumably due to the stronger contractions (Fig. S3C). The analysis of an *unc-105::GFP* knock-in strain revealed a widely distributed expression of UNC-105, which did not appear to be exclusively located in muscle cells (Fig. S3B). Overall, these results reveal a novel role for UNC-105 during embryonic elongation, which is important for relaxing muscle after contraction.

A model for the coordination of muscle contraction

Taken together, our results show that intestinal cells are involved in the morphogenesis of the embryo during the second stage of elongation. This new role for gut cells in the overall elongation of the embryo highlights the requirement for cells of the three germ layers in ensuring proper morphogenesis. The nature of the signal initiating muscle contractions and the molecular mechanism by which intestinal cells control muscle activity will await further studies. Indeed, we could not visualize the calcium exchange between intestinal and muscle cells (data not shown), even if they are in close proximity (Fig. 3E). One possibility is that other ions than Ca^{++} are involved, such as H^{+} ions as in defecation (Pfeiffer *et al.*, 2008; Wagner *et al.*, 2011), or that the probes used in the experiment were not sensitive enough. Previous work on *elt-2* mutants did not report an elongation arrest (Fukushige, *et al.*, 1998), yet a small size reduction as observed in *inx-15* mutants could have been missed.

The simplest model to explain why cell-2 and cell-3 behave like cells-1/4/5 in *inx-18* and *inx-15* mutants is that a signal emitted by intestinal cells through INX-15 singles out cell-2 and cell-3 (Fig. S4), which in turn activate cells-1/4/5. This model account for the fact that *inx-15* and *inx-18* are acting in the same pathway and for the respective localization of both proteins. In addition, INX-18 could be involved in communication between muscle cells. The signal transmitted by INX-15 and INX-18, and its propagation, subsequently require the Deg/Enac channels DEG-1 and UNC-105 to synchronize muscle cell activity in one quadrant. As DEG-1 is located at the interface between muscle cells and the surrounding collagen matrix, we could hypothesize that its opening in response to mechanical input balances and retro-controls muscle activity to allow muscle cell coordination dynamics (Liu, et al, 1996; Yan *et al.*, 2020).

In summary, this analysis highlights the role of adjacent cell bioelectric coupling, involving gap junctions and Deg/Enac channels, in facilitating cooperation between different connected tissues.

Figure Legends

Figure 1. Embryonic muscle activity. (A) Scheme of elongation depicting the lateral epidermal cells (purple) and the dorso-ventral cells (green). Red rectangle, time focus of the study. The cross-section below shows the relative positions of muscle cells (blue) just underneath the dorso-ventral epidermis, with the hemidesmosomes (red). **(B)** Snapshots from a timelapse showing muscle activity in an embryo labelled with GCaMP::GFP. T=0, time of the highest intensity. **(C)** Image of a two-fold embryo showing the GCaMP::GFP in the five cells with the first and highest fluorescence levels within in each muscle quadrant. **(D)** Correlation between muscle contractions (cell-1/-3 distance) in blue, and the normalized GCaMP::GFP intensity of cell-3 in light orange (n=7 embryos, 14 waves); the calcium peak is at 0.89 s before the contraction peak. T*, time of minimal distance between cell-1/3 (sec) (blue arrowhead). **(E)** Graph showing the calcium wave starting in cells-2/3 and propagating to cells-1/4/5. I_0 is the initial fluorescence intensity of each cell. In (D-E), dotted lines, average; shadow areas, standard error of the mean (SEM). **(F)** Dot plot showing the delay between Ca^{++} pulses among the five cells 1-5 (n=7 embryos, 14 waves); the cell pulsing first is in red for a given embryo. **(G)**. Normalized GCaMP::GFP maximum intensity relative to the b baseline fluorescence(I_b) for each cell. I_b is the baseline fluorescence intensity that is chosen as the lowest value of the intensity among the 5 cells in one wave **(H)** Normalized intensity versus the delay in pulsing (n=7 embryos, 14 waves)

Figure 2. Cell-2 and cell-3 behave as a pacemaker for muscle activity. (A) Snapshot of a timelapse showing a control embryo (top), and an embryo (bottom) in which cells-2 and cell-3 were photoablated in the dorsal and ventral left quadrants (black dotted lines). Yellow dotted line, embryo contours. **(B)** Localisation of the orange line used for building the kymograph. **(C)** Kymograph for control (top) and ablated cell-2/3 (bottom). The intensity was measured along the blue line. **(D)** Graph presenting the intensity over time. **(E)** Graph presenting the lengthening of the embryo over time (control, n=12 embryos; cell-2/3, n=8 embryos **(F)** Scheme of an embryo representing the different ROIs used for photoablation (outside, n=12 embryos; cell-2/3, n=12 embryos; anterior muscles, n=7 embryos; tails muscles, n=12 embryos). p-values, *,p<0,05 ***, p<0,0001.

Figure 3. Innexin roles in muscle activity. **(A)** *Pmyo-3::inx-18*::GFP expression in muscles. Note the dotty pattern outlining muscle cells. **(B-D)** Graphs detailing muscle GCaMP in wild type (black dots; data from Fig. 1), *inx-18(RNAi)* (purple dots, n=10 embryos and 19 waves), and *inx-18(ok2454)* (red dots, n=6 embryos and 14 waves) embryos, showing delay in pulsing (B), peak intensity (C), pulse contraction duration (D). **(E)** Embryo showing *Pelt-2*::INX-15::mCherry and *Pmyo-3*::PH::GFP localization. **(F-H)** Graphs detailing muscle activity in wild type (black dots; data from Fig. 1), *inx-15(RNAi)* (yellow dots, n=5 embryos and 12 waves), and *inx-15(syb5414)* (brown dots, n=6 embryos and 14 waves) embryos, showing delay in pulsing (F), peak intensity (G), pulse contraction duration (H). **(I)** Plot of intensity versus delays in wild type, *inx-18(ok2454)* and *inx-15(syb5414)* embryos. **(J)** Elongation curves of wild type, *inx-15(RNAi)*, *inx15(syb5414), inx-15(syb5414);inx-18(ok2454)* and *pak-1(tm403)* embryos. **(K)** Length of wildtype, *inx-15(syb5414); Pelt-2*::INX-15::mCherry, and *inx15(syb5414*) hatching L1 larvae (n=32 hatching larvae for all conditions). P-values, ***, p<0,0001 .

Figure 4. DEG/ENac channels are required for normal muscle activity. (A-C) GCaMP activity analysis showing the delay in pulsing (A), the intensity of the

pulses (B) and the duration of the pulses (C) for wild-type (black dots; data from Fig. 1), *unc-105(n506)* (blue dots, n=8 embryos and 10 waves) and *deg-1(u506)* (red dots; n=8 embryos, 13 waves) **(D)** Plot of intensity versus delay of wild type, *deg-1(u506)* and *unc-105(n506)* embryos. **(E)** Elongation curve for *deg-1(n506)* (n=9) and wild-type(n=10) at 16°C**. (F)** Elongation curve for *unc-105(n506)* (n=6) and wild-type (n=12) at 20°C. (**G)** Localisation of DEG-1::GFP in muscle cells labelled with a *Pmyo-3*::mCherry transgene. **(G1)** Transversal view of the image in G. Data in E-F represent mean values ± SEM.

Materials and methods

Strains

Animals were grown on NGM (nematode growth medium) plates with a bacterial lawn of the OP50 E. coli strain, following the protocol of Brenner (1974) and generally maintained at 20°C unless otherwise stated for temperature sensitive mutants. The alleles *deg-1(syb5346)*, strain PHX5346, *inx-15(syb5728)*, strain PHX5728 and *unc-105(syb4276)*, strain PHX4276, as well as the knockin *deg-1::GFP(syb4251)*, strain PHX4251, and were generated by Suny Biotech (Fu Jian Province, China; https://www.sunybiotech.com/) using the CRISPR/CAS9 technology (table S3).

RNAi mini-screen

RNAi was performed by feeding L4 hermaphrodites with HT115 E. coli expressing dsRNA. 41 dsRNA cloned in the L440 vectors came from the Ahringer's library were sequenced to confirm the target gene. The other dsRNAs were cloned into the L440 vector after amplification of the sequence using the appropriate set of primers (table S3), and subsequent transformation in HTT115 E. *coli*. L4 animals were fed during 24 h or 48 h hours prior to the analysis the progeny.

Real-time calcium intensity analysis

The embryos were mounted on a glass slide over a 2% agarose pad with the M9 buffer (86 mM NaCl, 42 mM Na2HPO4, 22 mM KH2PO4, 1 mM MgSO4). Embryos were observed with a Zeiss Axio Observer.Z1 inverted spinning disk microscope equipped with a *CSUX1-A1* (Yokogawa) spinning disc module, a Roper Evolve camera and an apochromatic oil-immersion 100x objective (NA=1.4). The microscope was controlled by the Metamorph (Molecular Devices) acquisition software. For long-time imaging of Pmyo3::PH::GFP membrane labeled muscle, excitation was set at 300 ms and 20 % of laser. For calcium imaging, a stream acquisition mode was used with 50 ms of excitation and 36,5 % of laser at 30 ms intervals. All live imaging experiments were

performed at 20°C, except for experiments involving *deg-1(u506)* which were performed at 16°C.

Photoablation experiment

To specifically ablate cells 2 and 3, we used a transgenic animal carrying the *pmyo3*::MiniSOG::mCherry construct which is active only in muscle cells. Just prior to the start of muscle activity, we designed an ROI (region of interest) for cells 2 and 3 in the ventral and dorsal quadrants, took two images 1 min and 30 s before photoablation. We then photoablated the two cells in each quadrants using the FRAP module of the ILAS software installed on the spinning disc with a 456 nm laser at 80% power for 2 min, and finally recorded muscle activity every 30s for 25 minutes. For the control experiment, we ablated an ROI located outside the myo-3 labelled cells, this ROI is a region without any labelling, it could correspond to the location of the neurons. This ROI is designed in the same z plane as the muscle cells.

Photo Ablation analysis

To quantify muscle activity and muscle twitching, we used the Image J software (NIH, Bethesda, Maryland, USA; http://rsb.info.nih.gov/ij/) to design a line passing through cells 2 and 3 and built a kymograph.

Analysis of elongation rate

DIC time-lapse videos were obtained using a Leica DM6000 microscope controlled by a Leica LAS-AF software. Observations were done under a 40X~ oil immersion objective. Mothers were cut up to gain early-staged embryos, which were then transferred onto thin 5% soft agarose pads in a drop of M9. Z-stack image series with a 1.5-µm Z-step distance were taken every 10 min during 16 h. The image J software was used to quantify the embryonic length from the end of ventral enclosure/onset of elongation, by taking a segmented line through the midline of the embryos from head to tail. For the *deg-1(u506)* mutant we set up the microscopy room at 16°C.

Fluorescence microscopy analysis

We acquired fluorescence images with a LSM 980 Airyscan2 Zeiss confocal system equipped with 488 nm and 561 nm excitation laser lines and a 63x oil immersion objective with NA 1,4 and 0,15 µm z-steps. In confocal mode, we performed a simultaneous acquisition for the green and red channels in order to get both markers at the same time. These images were deconvoluted with the Huygens software, then analyzed single plane images or max z projection images using the Image J software.

Calcium image analysis

We performed maximal projection along z of the original time-dependent movies of HBR4 and corrected them for photobleaching by using the dedicated exponential correction tool in FIJI. Subsequently, we used a Matlab script to measure the average fluorescence intensity in cell cytoplasm by hand-tracking the cells contours by using the *roipoly* function (ROI, region of interest). In each embryo we monitored and tracked the average fluorescence of five muscle's cells below the H1, H2, v1 cells. Moreover, we recorded the spatial coordinates of the center of mass of each ROI. We converted the spatial coordinates in curvilinear abscissa with respect to the anterior-posterior (AP) axis after manually tracing the body midline from the tip of the embryo head to the tip of the tail. To isolate pulses of signal in a selected cell, we plotted the behavior of the average fluorescence in time. We observed that the signal intensity increased with respect to its baseline within a few seconds, reached a maximum and then decreased again to a value similar to the initial baseline. The resulting time behavior was similar to a bell shape. Indeed, we observed that a pulse in a cell was coordinated with pulses in neighboring cells, which tend to pulse in a group producing a wave of calcium signal. We decided to characterize a single pulse by its initiation time, its termination time and Its duration. The initiation time was calculated as the time at which the calcium pulse intensity reaches 30% of its maximum, as illustrated in Fig. 1D. It was calculated on the intensity normalized between 0 and 1 by subtracting the initial intensity I_0 which is the initial fluorescence intensity of each cell from I(t)

and dividing by the maximum of $I(t)-I_0$. The termination time was defined as the time at which the normalized intensity decreased till 30% of its maximum after reaching its maximum. The choice of the threshold of 30% is arbitrary. The duration of a calcium pulse is calculated as the difference between the termination time and the initiation time of the normalized intensity.

To characterize the coordination of the pulses between neighboring cells we measured the delay in pulsing between different cells and the speed of the calcium wave. We estimated the delay with respect to the cell among the five cells pulsing first. More precisely the delay in pulse was defined as the difference in the initiation time with the first pulsing cell. We measured the average wave velocity as $v_w = abs(\langle x_{last}\rangle - \langle x_{first}\rangle)/(\langle t_{last}\rangle - \langle t_{first}\rangle)$, where $(\langle t_{last}\rangle - \langle t_{first}\rangle)$ is the difference between the average delay at which the first cell ($\langle t_{first}\rangle$) pulsed and the average delay at which pulse the last cell ($\langle t_{last}\rangle$); $abs(\langle x_{last}\rangle - \langle x_{first}\rangle)$ is the modulus of the difference between the average AP position of the last pulsing cell $\langle x_{last}\rangle$ and the average AP position of the first pulsing cell $\langle x_{first}\rangle$. inally, we characterized the intensity of the pulses by measuring the peak intensity as the maximal intensity reached by a cell during a pulse normalized with respect to the minimal baseline value of the intensity I_b measured among the selected five cells. More precisely we defined $I_{peak} = (I_{max} - I_b)/ - I_b$. Peak $[(I-I_b)/I_b]$ where I_b is the baseline fluorescence intensity that is chosen as the lowest value of the intensity among the 5 cells in one wave.

Statistical analysis

For elongation curves, the standard error of the mean (SEM) was calculated. For L1 hatching measurements and ablation intensity, we performed paired t-tests or ANOVA test using the GraphPad PRISM software. For calcium analysis, all the analyses were done using MATLAB (The MathWorks Inc., Natick, MA). All the p values are in table S2.

Supplementary Figure legends

Supplementary Figure 1. Characterization of the first contracting muscles. (A) Fluorescent embryo showing the respective localization of cell-2 and cell-3 (*Pmyo-3*::GCaMP::GFP) compared to pharynx PHA-4::GFP positive cells(arrow). **(B)** Fluorescent embryo showing the respective localization of cell-2 and cell-3 (*Pmyo-3*::GCaMP::GFP) compared to epidermal DLG-1::RFP positive cells. **(C)** Fluorescence micrographs showing muscle quadrant connections labelled with *Pmyo-3*::pH::GFP**.** Dorsal/dorsal connections and dorsal/ventral connections were always observed, whereas ventral/ventral connections were rarely observed. Scale bar, 10µm**. (D)** Quantification of the number of connections (n=24 embryos). **(E)** Contraction frequency (number contraction/minute) in *wild type*, *deg-1(u506)*, *unc-105(n506), inx15(syb5414)*, and *inx-18(ok2454)*. **(F)** Propagation speed of the calcium wave in *wild type*, *unc-105(n506), inx15(syb5414)*, and *inx-18(ok2454)* embryos. P-values, *, p<0,01

Supplementary Figure 2. **Additional characterization of INX-15 and INX-18.** **(A-B)** Embryos labelled with the *Pmyo-3*::pH::GFP in control (A) *and inx-18(RNAi)* background (B). **(C)** Embryo showing the *Pinx-15::GFP* transcriptional reporter profile. **(D)** Distribution of a *Pinx-18::gfp* translational reporter. **(E-F)** Graphs showing the delay in GCaMP::GFP pulsing (E), and the intensity of the pulses (F) for wild-type, *inx-18(ok2454)*, *inx-15(syb5414)*and *inx-15(syb5414);inx-18(ok2454)* embryos. Scale bar, 10µm**.**

Supplementary Figure 3. Additional characterization of DEG-1 and UNC-105. **(A)** images of DEG-1::GFP (green), EMB-9::mCherry (red), and merge. **(B)** images of UNC-105::GFP (green), EMB-9::mCherry (red), and merge. Scale bar, 10µm**. (C)** Graphs showing the correlation between muscle contraction

(distance between cell1 and cell3) in blue and the normalized Calcium sensor intensity of cell-3 in light orange in wild type, *deg-1(u506)* and *unc-105(n506)*. .T, time (sec); T*, time of minimal distance between cell-1 and -3 (sec)

Supplementary Figure 4. **A model for the coordination of muscle activity in embryos.** The proposed model involves an unknown signal implicating INX-15 in intestinal cells (blue), which preferentially activates muscle cells-2 and -3 through INX-18. Of note, how muscle cells initiate their activity remains unknown. INX-18 facilitates signal propagation and activates surrounding muscle cells Within the muscle quadrant, the activities of DEG-1 and UNC-105 (orange) are essential for maintaining synchronization between muscle cells and aiding signal propagation. Together, these interactions among the three tissues ensure proper embryo elongation at the level of the epidermal cells.

Supplementary Movie 1: Movie of an embryo showing the GCaMP::GFP in the five cells with the first and highest fluorescence levels within in each muscle quadrant. Scale bar, 10µm.

Supplementary Movie 2: Movie of an embryo showing muscle quadrant connections labelled with *Pmyo-3*::pH:: miniSOG. Scale bar, 10µm.

Supplementary Movie 3: Movie of a control embryo (left), and an embryo (right) in which t cell-2 and cell-3 were photoablated in the dorsal and ventral left quadrants expressing the *Pmyo-3*::PH::miniSOG. Note how the control embryo, but not the ablated embryo, rotates within the eggshell. Scale bar, 10µm.

Acknowledgements

The authors thank Jean-Louis Bessereau for his careful reading of the manuscript, Caenorhabditis Genetics Center (funded by the NIH Office of

Research Infrastructure Programs P40 OD010440), Sunybiotech , Andrew D. Chisholm, Henrik Bringmann, Jihong Bai, Shinji Ihara for strains, Jihong Bai, Henrik Bringmann for reagents, and the IBPS imaging center for advice. This work was supported by grants from the Agence Nationale pour la Recherche (grant #ANR-18-CE13-0008-01) and the Association pour la Recherche sur le Cancer (Subvention 2018).

Competing interests

The authors declare no competing or financial interests.

Authors' contributions

FL and ML conceived the project and wrote the manuscript. FL performed most experiments; TF performed Ca++ quantifications, XY quantified embryo rotations and HL the connections between muscle quadrants.

REFERENCES

Alfonso, A. *et al.* (1993) 'The Caenorhabditis elegans unc-17 gene: a putative vesicular acetylcholine transporter.', *Science (New York, N.Y.)*, 261(5121), pp. 617–619. Available at: https://doi.org/10.1126/science.8342028.

Altun ZF, Chen B, Wang ZW, Hall DH. High resolution map of Caenorhabditis elegans gap junction proteins. Dev Dyn. 2009 Aug;238(8):1936-50. doi: 10.1002/dvdy.22025. Erratum in: Dev Dyn. 2015 Jul;244(7):903. doi: 10.1002/dvdy.24287. PMID: 19621339; PMCID: PMC2732576.

Eastwood, A.L. and Goodman, M.B. (2012) 'Insight into DEG/ENaC channel gating from genetics and structure.', *Physiology (Bethesda, Md.)*, 27(5), pp. 282–290. Available at: https://doi.org/10.1152/physiol.00006.2012.

Fukushige, T., Hawkins, M.G. and McGhee, J.D. (1998) 'The GATA-factor elt-2 is essential for formation of the Caenorhabditis elegans intestine.', *Developmental biology*, 198(2), pp. 286–302.

García-Añoveros, J., Ma, C. and Chalfie, M. (1995) 'Regulation of Caenorhabditis elegans degenerin proteins by a putative extracellular domain.', *Current biology : CB*, 5(4), pp. 441–448. Available at: https://doi.org/10.1016/s0960-9822(95)00085-6.

Geffeney, S.L. *et al.* (2011) 'DEG/ENaC but not TRP channels are the major mechanoelectrical transduction channels in a C. elegans nociceptor.', *Neuron*, 71(5), pp. 845–857. Available at: https://doi.org/10.1016/j.neuron.2011.06.038.

Gieseler, K., Qadota, H. and Benian, G.M. (2017) 'Development, structure, and maintenance of C. elegans body wall muscle.', *WormBook : the online review of C. elegans biology*, 2017, pp. 1–59. Available at: https://doi.org/10.1895/wormbook.1.81.2.

Lardennois, A. *et al.* (2019) 'An actin-based viscoplastic lock ensures progressive body-axis elongation.', *Nature*, 573(7773), pp. 266–270. Available at: https://doi.org/10.1038/s41586-019-1509-4.

Liu, J., Schrank, B. and Waterston, R.H. (1996) 'Interaction between a putative mechanosensory membrane channel and a collagen.', *Science (New York, N.Y.)*, 273(5273), pp. 361–364. Available at: https://doi.org/10.1126/science.273.5273.361.
Liu, P. *et al.* (2013) 'Six innexins contribute to electrical coupling of C. elegans body-wall muscle.', *PloS one*, 8(10), p. e76877. Available at: https://doi.org/10.1371/journal.pone.0076877.
Mitchell, N.P. *et al.* (2022) 'Visceral organ morphogenesis via calcium-patterned muscle constrictions.', *eLife*, 11. Available at: https://doi.org/10.7554/eLife.77355.
Moyle, M.W. *et al.* (2021) 'Structural and developmental principles of neuropil assembly in C. elegans.', *Nature*, 591(7848), pp. 99–104. Available at: https://doi.org/10.1038/s41586-020-03169-5.
Nelson, C.M. and Gleghorn, J.P. (2012) 'Sculpting Organs: Mechanical Regulation of Tissue Development', *Annual Review of Biomedical Engineering*. Annual Reviews. Available at: https://doi.org/10.1146/annurev-bioeng-071811-150043.
Nonet, M.L *et al*. (1998) ' Synaptic Transmission Deficits in Caenorhabditis elegans Synaptobrevin Mutants.', The Journal of Neuroscience, January 1, 1998, 18(1):70–80. 10.1523/JNEUROSCI.18-01-00070.1998.
Park, E.C. and Horvitz, H.R. (1986) 'C. elegans unc-105 mutations affect muscle and are suppressed by other mutations that affect muscle.', *Genetics*, 113(4), pp. 853–867. Available at: https://doi.org/10.1093/genetics/113.4.853.
Peters, M.A. *et al.* (2007) 'A calcium wave mediated by gap junctions coordinates a rhythmic behavior in C. elegans.', *Current biology : CB*, 17(18), pp. 1601–1608. Available at: https://doi.org/10.1016/j.cub.2007.08.031.
Pfeiffer, J., Johnson, D. and Nehrke, K. (2008) 'Oscillatory transepithelial H(+) flux regulates a rhythmic behavior in C. elegans.', *Current biology : CB*, 18(4), pp. 297–302. Available at: https://doi.org/10.1016/j.cub.2008.01.054.
Schwarz, J., Spies, J.-P. and Bringmann, H. (2012) 'Reduced muscle contraction and a relaxed posture during sleep-like Lethargus.', *Worm*, 1(1), pp. 12–14. Available at: https://doi.org/10.4161/worm.19499.
Shah, P.K. *et al.* (2017) 'PCP and SAX-3/Robo Pathways Cooperate to Regulate Convergent Extension-Based Nerve Cord Assembly in C. elegans.', *Developmental cell*, 41(2), pp. 195-203.e3. Available at: https://doi.org/10.1016/j.devcel.2017.03.024.
Simonsen, K.T., Moerman, D.G. and Naus, C.C. (2014) 'Gap junctions in C. elegans.', *Frontiers in physiology*, 5, p. 40. Available at: https://doi.org/10.3389/fphys.2014.00040.
Takagaki, N. *et al.* (2020) 'The mechanoreceptor DEG-1 regulates cold tolerance in Caenorhabditis elegans.', *EMBO reports*, 21(3), p. e48671. Available at: https://doi.org/10.15252/embr.201948671.
Viveiros, R., Hutter, H. and Moerman, D.G. (2011) 'Membrane extensions are associated with proper anterior migration of muscle cells during Caenorhabditis elegans embryogenesis.', *Developmental biology*, 358(1), pp. 189–200. Available at: https://doi.org/10.1016/j.ydbio.2011.07.026.
Voelker, L. *et al.* (2019) 'INX-18 and INX-19 play distinct roles in electrical synapses that modulate aversive behavior in Caenorhabditis elegans.', *PLoS genetics*, 15(10), p. e1008341. Available at: https://doi.org/10.1371/journal.pgen.1008341.
Vuong-Brender, T.T.K. *et al.* (2017) 'The interplay of stiffness and force anisotropies drives embryo elongation.', *eLife*, 6, p. e23866. Available at: https://doi.org/10.7554/eLife.23866.
Vuong-Brender, T.T.K., Yang, X. and Labouesse, M. (2016) 'C. elegans Embryonic Morphogenesis.', *Current topics in developmental biology*, 116, pp. 597–616. Available at: https://doi.org/10.1016/bs.ctdb.2015.11.012.
Wagner, J. *et al.* (2011) 'A calcineurin homologous protein is required for sodium-proton

exchange events in the C. elegans intestine.', *American journal of physiology. Cell physiology*, 301(6), pp. C1389-1403. Available at: https://doi.org/10.1152/ajpcell.00139.2011.
Wu, Y. *et al.* (2011) 'Inverted selective plane illumination microscopy (iSPIM) enables coupled cell identity lineaging and neurodevelopmental imaging in Caenorhabditis elegans.', *Proceedings of the National Academy of Sciences of the United States of America*, 108(43), pp. 17708–17713. Available at: https://doi.org/10.1073/pnas.1108494108.
Xu, S. and Chisholm, A.D. (2016) 'Highly efficient optogenetic cell ablation in C. elegans using membrane-targeted miniSOG.', *Scientific reports*, 6, p. 21271. Available at: https://doi.org/10.1038/srep21271.
Yan, Z. *et al.* (2020) 'Caenorhabditis elegans body wall muscles sense mechanical signals with an amiloride-sensitive cation channel.', *Biochemical and biophysical research communications*, 527(2), pp. 581–587. Available at: https://doi.org/10.1016/j.bbrc.2020.04.130.
Zhang, H. *et al.* (2011) 'A tension-induced mechanotransduction pathway promotes epithelial morphogenesis.', *Nature*, 471(7336), pp. 99–103. Available at: https://doi.org/10.1038/nature09765.
Zinner, M., Lukonin, I. and Liberali, P. (2020) 'Design principles of tissue organisation: How single cells coordinate across scales.', *Current opinion in cell biology*, 67, pp. 37–45. Available at: https://doi.org/10.1016/j.ceb.2020.07.004.

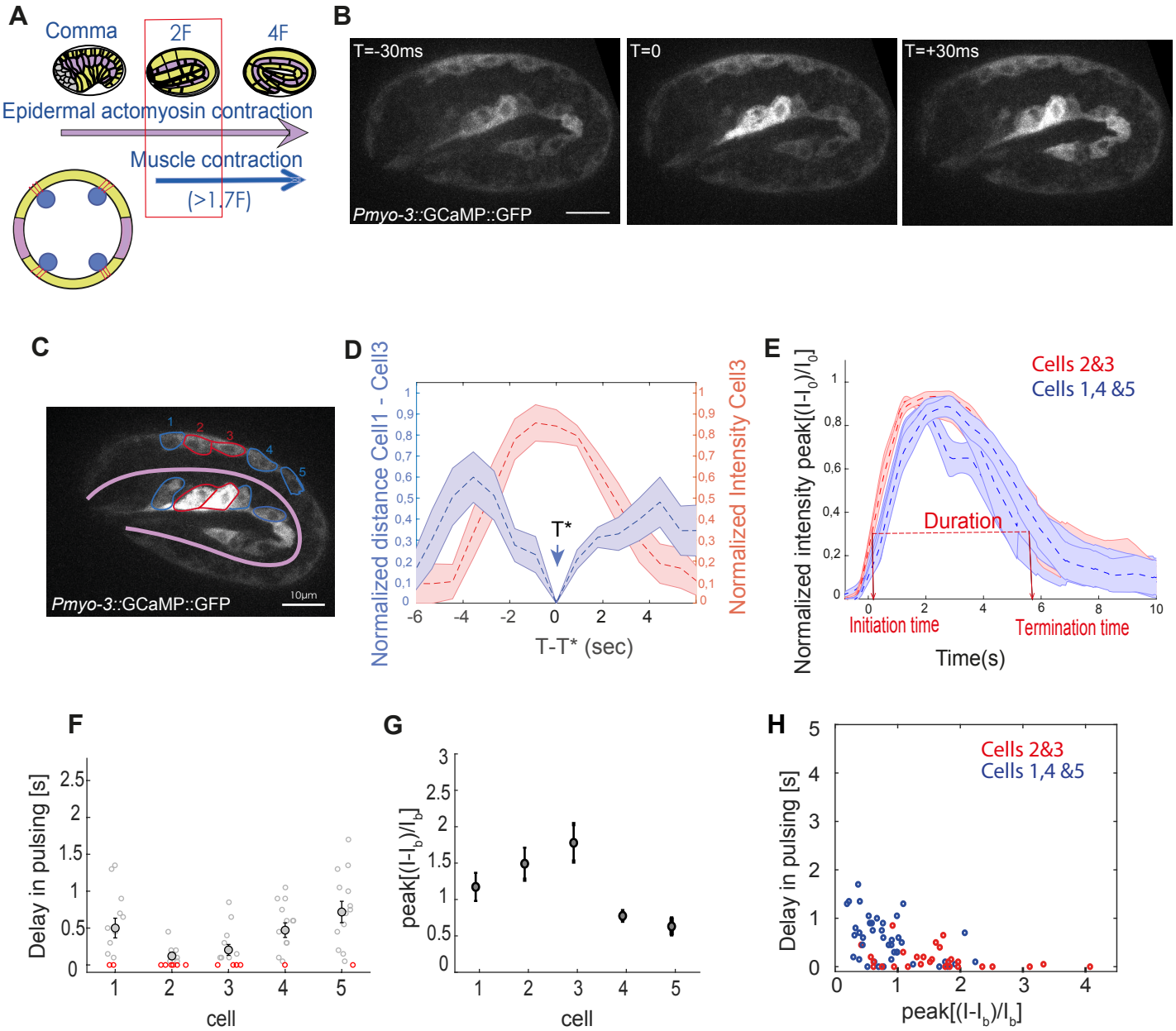
A
Comma
2F
4F
Epidermal actomyosin contraction
Muscle contraction
(>1.7F)
B
T=-30ms
T=0
T=+30ms
Pmyo-3::GCaMP::GFP
C
Pmyo-3::GCaMP::GFP
10µm
D
Normalized distance Cell1 - Cell3
Normalized Intensity Cell3
T*
T-T* (sec)
E
Cells 2&3
Cells 1,4 &5
Normalized intensity peak[(I-I0)/I0]
Duration
Initiation time
Termination time
Time(s)
F
Delay in pulsing [s]
cell
G
peak[(I-Ib)/Ib]
cell
H
Cells 2&3
Cells 1,4 &5
Delay in pulsing [s]
peak[(I-Ib)/Ib]

Figure 1

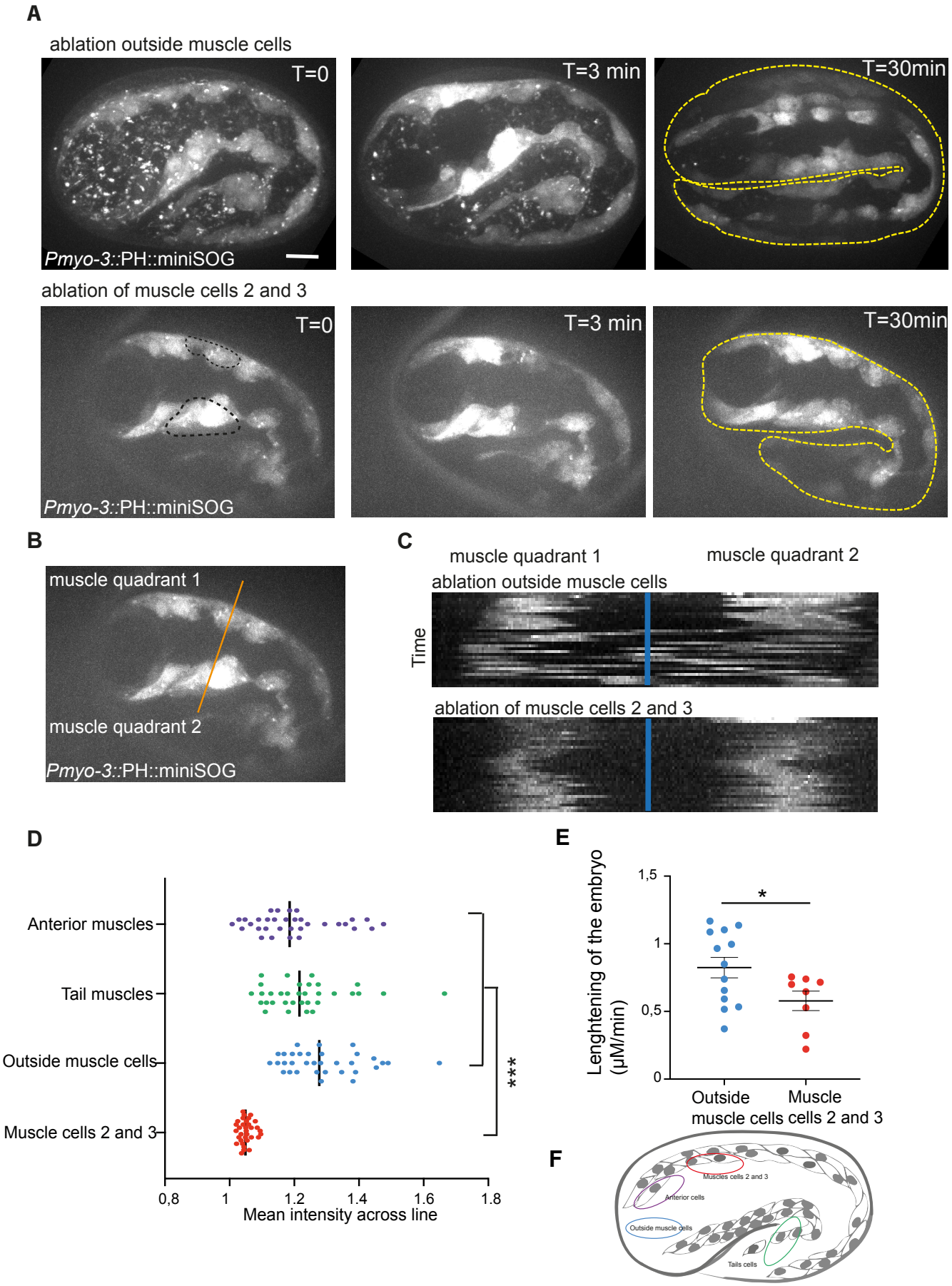
A
ablation outside muscle cells
T=0
T=3 min
T=30min
Pmyo-3::PH::miniSOG
ablation of muscle cells 2 and 3
T=0
T=3 min
T=30min
Pmyo-3::PH::miniSOG
B
muscle quadrant 1
muscle quadrant 2
Pmyo-3::PH::miniSOG
C
muscle quadrant 1
muscle quadrant 2
ablation outside muscle cells
Time
ablation of muscle cells 2 and 3
D
Anterior muscles
Tail muscles
Outside muscle cells
Muscle cells 2 and 3
***
0,8
1
1.2
1.4
1.6
1.8
Mean intensity across line
E
Lenghtening of the embryo (µM/min)
1,5
1
0,5
0
*
Outside muscle cells
Muscle cells 2 and 3
F
Muscles cells 2 and 3
Anterior cells
Outside muscle cells
Tails cells

Figure 2

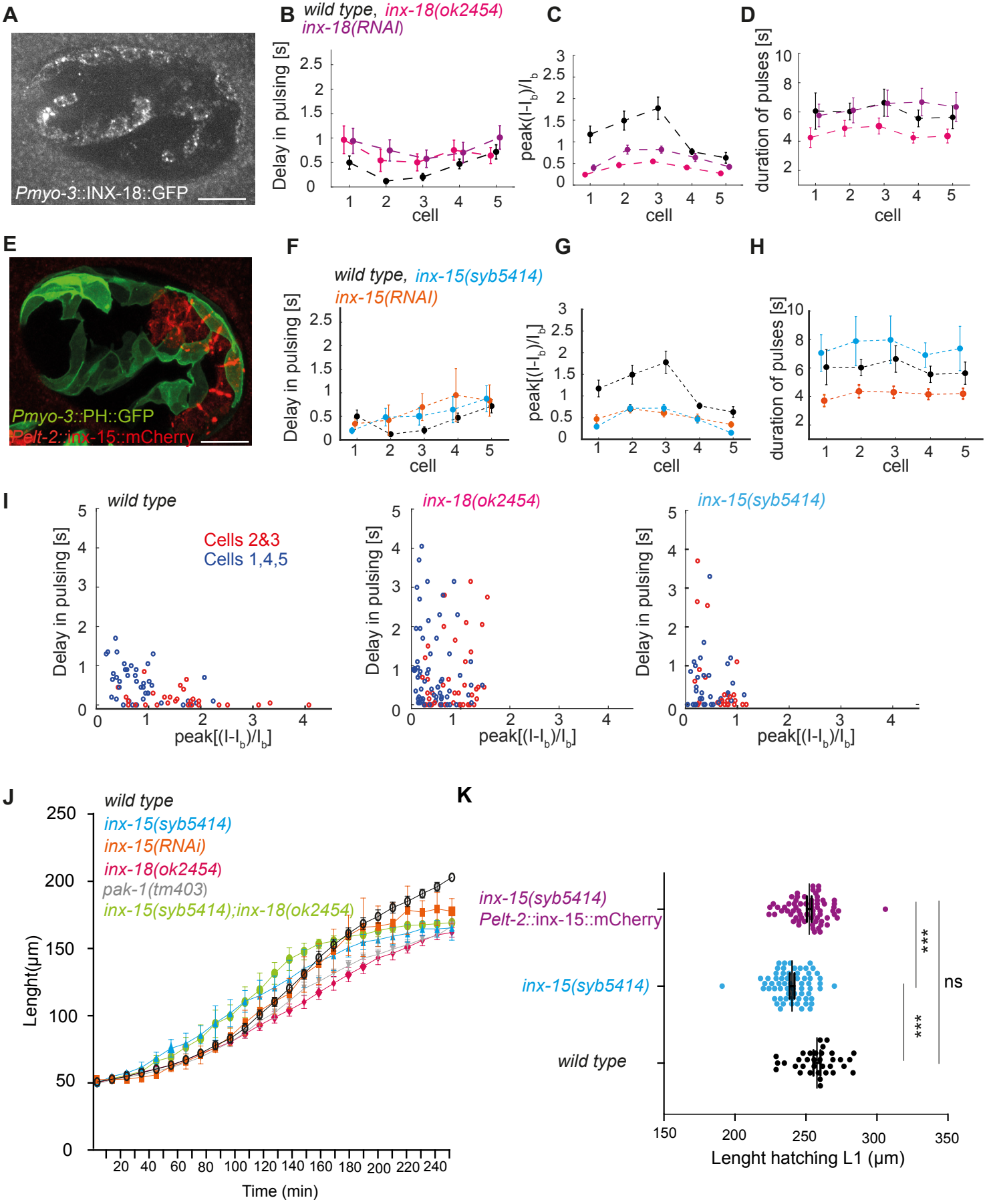
A
Pmyo-3::INX-18::GFP
B
wild type, inx-18(ok2454)
inx-18(RNAI)
Delay in pulsing [s]
cell
C
peak(I-I_b)/I_b
cell
D
duration of pulses [s]
cell
E
Pmyo-3::PH::GFP
Pelt-2::inx-15::mCherry
F
wild type, inx-15(syb5414)
inx-15(RNAI)
Delay in pulsing [s]
cell
G
peak[(I-I_b)/I_b]
cell
H
duration of pulses [s]
cell
I
wild type
Cells 2&3
Cells 1,4,5
inx-18(ok2454)
inx-15(syb5414)
Delay in pulsing [s]
peak[(I-I_b)/I_b]
J
wild type
inx-15(syb5414)
inx-15(RNAi)
inx-18(ok2454)
pak-1(tm403)
inx-15(syb5414);inx-18(ok2454)
Lenght(µm)
Time (min)
K
inx-15(syb5414)
Pelt-2::inx-15::mCherry
inx-15(syb5414)
wild type
***
***
ns
Lenght hatching L1 (µm)

Figure 3

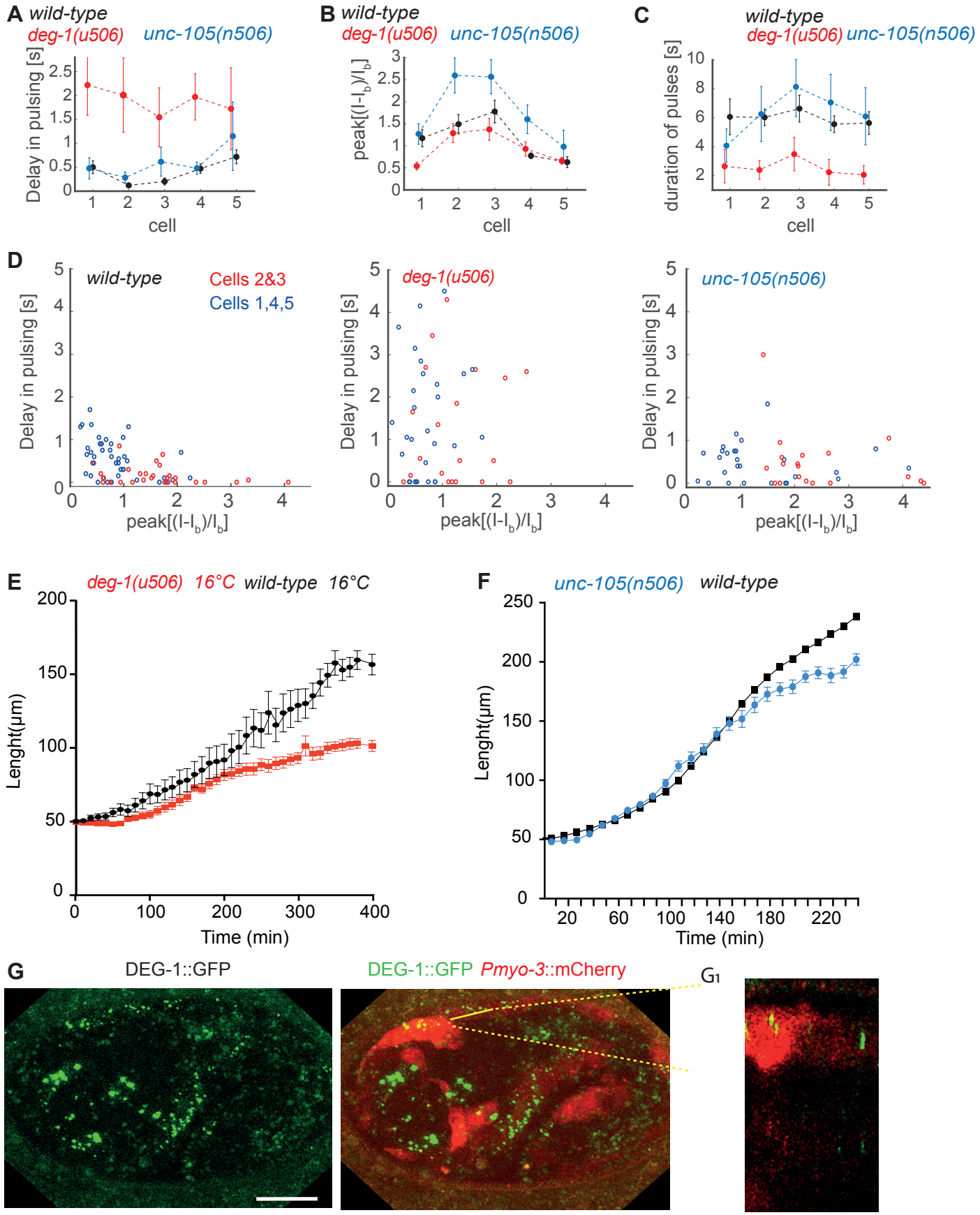
A
wild-type
deg-1(u506)
unc-105(n506)
Delay in pulsing [s]
cell
B
wild-type
deg-1(u506)
unc-105(n506)
peak[(I-I_b)/I_b]
cell
C
wild-type
deg-1(u506)
unc-105(n506)
duration of pulses [s]
cell
D
wild-type
Cells 2&3
Cells 1,4,5
deg-1(u506)
unc-105(n506)
Delay in pulsing [s]
peak[(I-I_b)/I_b]
E
deg-1(u506) 16°C
wild-type 16°C
Lenght(µm)
Time (min)
F
unc-105(n506)
wild-type
Lenght(µm)
Time (min)
G
DEG-1::GFP
DEG-1::GFP Pmyo-3::mCherry
G1

Figure 4

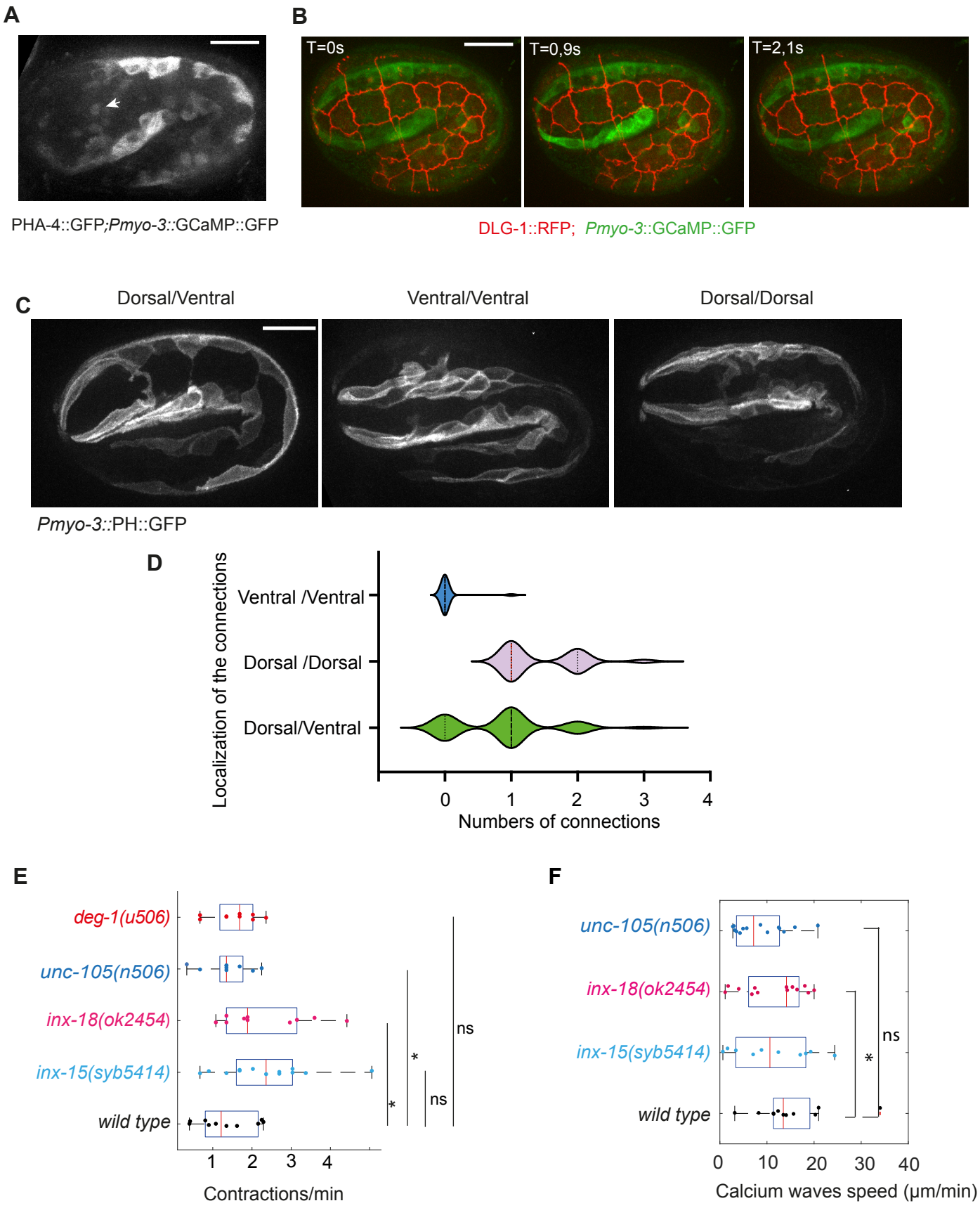
A
PHA-4::GFP;Pmyo-3::GCaMP::GFP
B
T=0s
T=0,9s
T=2,1s
DLG-1::RFP; Pmyo-3::GCaMP::GFP
C
Dorsal/Ventral
Ventral/Ventral
Dorsal/Dorsal
Pmyo-3::PH::GFP
D
Localization of the connections
Ventral /Ventral
Dorsal /Dorsal
Dorsal/Ventral
0
1
2
3
4
Numbers of connections
E
deg-1(u506)
unc-105(n506)
inx-18(ok2454)
inx-15(syb5414)
wild type
*
*
ns
ns
1
2
3
4
Contractions/min
F
unc-105(n506)
inx-18(ok2454)
inx-15(syb5414)
wild type
ns
*
0
10
20
30
40
Calcium waves speed (µm/min)

Figure S1

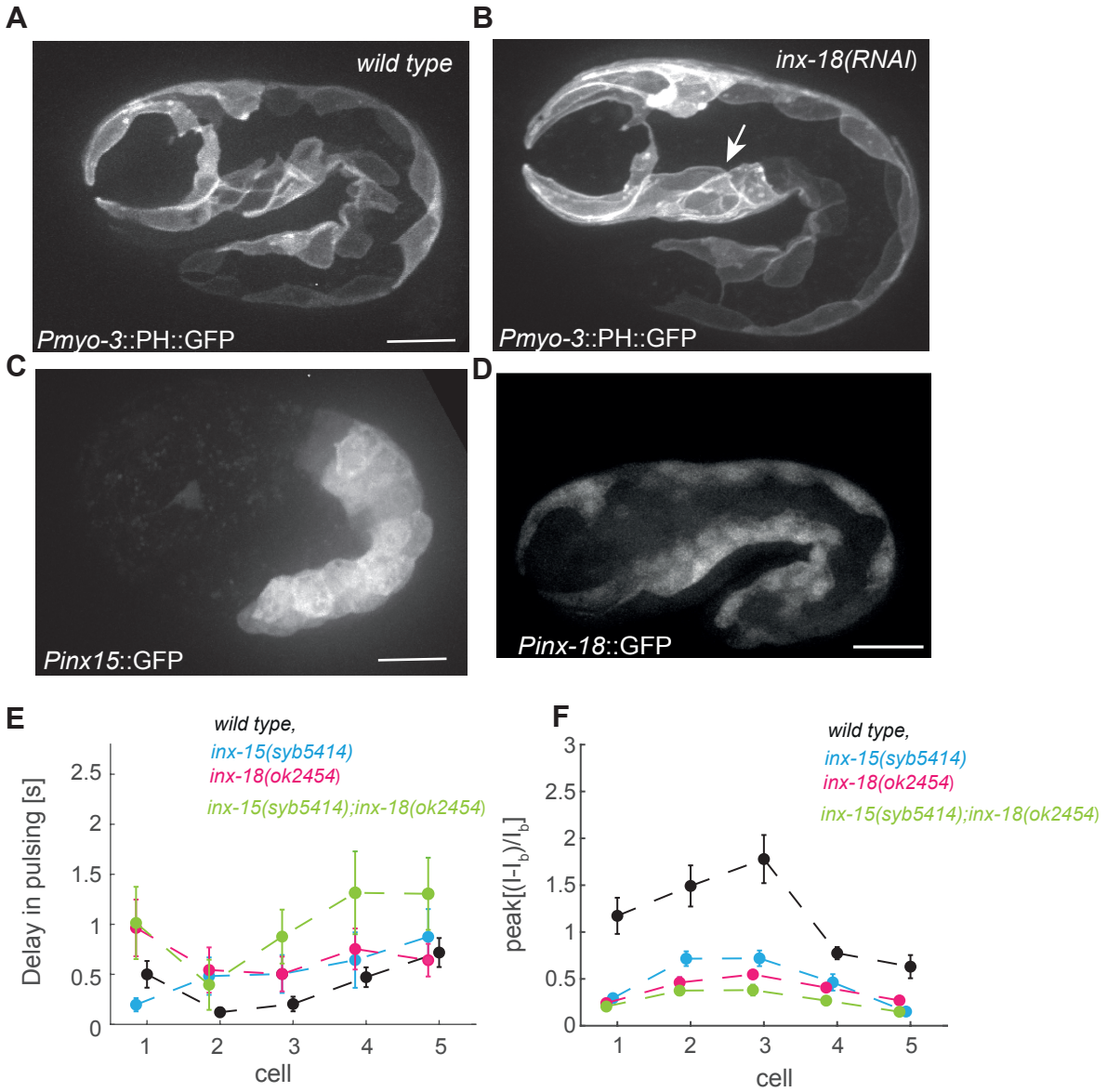
A
wild type
Pmyo-3::PH::GFP
B
inx-18(RNAI)
Pmyo-3::PH::GFP
C
Pinx15::GFP
D
Pinx-18::GFP
E
wild type,
inx-15(syb5414)
inx-18(ok2454)
inx-15(syb5414);inx-18(ok2454)
Delay in pulsing [s]
cell
F
wild type,
inx-15(syb5414)
inx-18(ok2454)
inx-15(syb5414);inx-18(ok2454)
peak[(I-I_b)/I_b]
cell

Figure S2

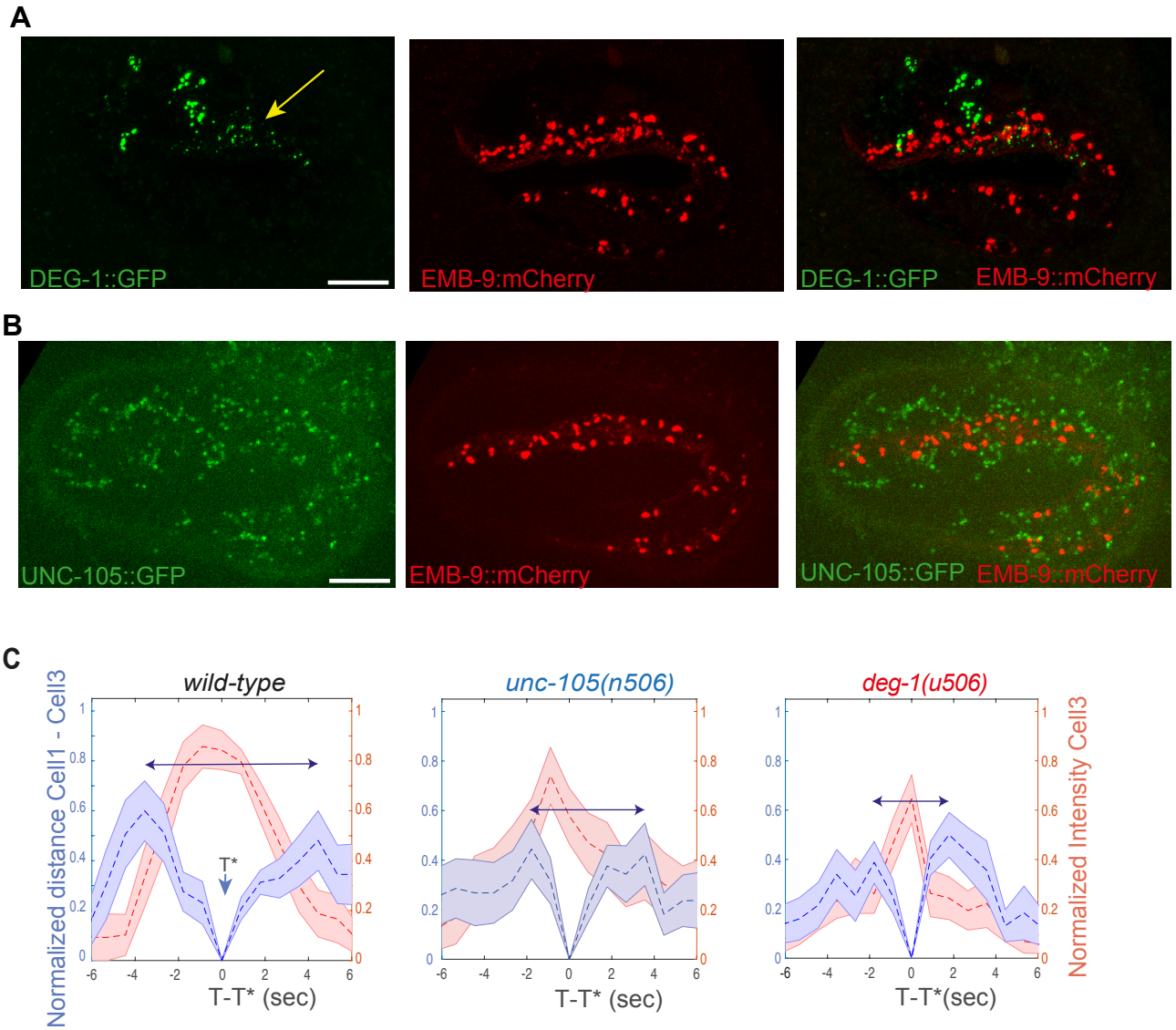
A
DEG-1::GFP
EMB-9:mCherry
DEG-1::GFP
EMB-9::mCherry
B
UNC-105::GFP
EMB-9::mCherry
UNC-105::GFP
EMB-9::mCherry
C
wild-type
unc-105(n506)
deg-1(u506)
Normalized distance Cell1 - Cell3
Normalized Intensity Cell3
T*
T-T* (sec)
T-T* (sec)
T-T*(sec)

Figure S3

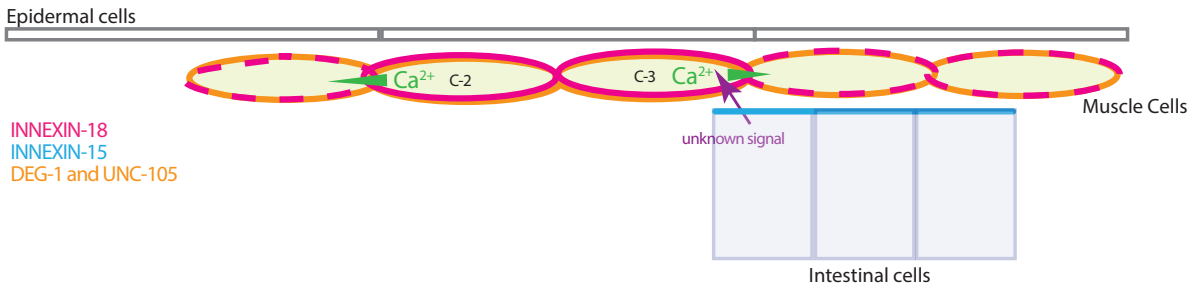
Epidermal cells
Ca2+
C-2
C-3
Ca2+
Muscle Cells
INNEXIN-18
INNEXIN-15
DEG-1 and UNC-105
unknown signal
Intestinal cells

Figure S4

Gene list	Homology	Phenotype
inx-12	Innexin 12	Normal
inx-13	Innexin13	Normal
inx-14	Innexin14	Normal
inx-15	Innexin15	muscle cell morphology abnormal
inx-16	Innexin16	Normal
inx-17	Innexin17	Normal
inx-19	Innexin19	Normal
inx-20	Innexin20	Normal
inx-21	Innexin21	Normal
inx-22	Innexin22	Normal
eat-5		Normal
inx-6	Innexin6	Normal
inx-7	Innexin7	Normal
inx-8	Innexin8	Normal
inx-9	Innexin9	Normal
inx-18	Innexin18	bump ventral side
inx-4 (che-7)	Innexin4	Normal
inx-10	Innexin10	Normal
inx-11	Innexin11	Normal
inx-1	Innexin1	Normal
inx-2	Innexin2	Normal
inx-3	Innexin3	Normal
inx-5	Innexin5	Normal
unc-9		Normal
unc-7	unc-7	Normal
mec-4	SCNN1B (sodium channel epithelial 1 subunit beta	Normal
mec-10	SCNN1B	Normal
unc-105	SCNN1B	Normal
del-1	SCNN1B	Normal
deg-1	SCNN1B	Normal
del-10	SCNN1B	NOT TESTED
unc-8	SCNN1B	Normal
Flr-1	ASIC	Normal

trp-1	TRPC	Normal
trp-3		NOT TESTED
cup-5	MCOLN1	NOT TESTED
gtl-1	TRPM	Normal
gtl-2	TRPM	Normal
trpa-1	TRPA	Normal
osm-9	TRPV	Normal
ocr-1	TRPV	Normal
gon-2	TRPM	Normal
trpa-2	TRPA	Normal
acd-1	ASIC	Normal
ocr-2	TRPV	Normal
Spc-1	SPTAN1	Muscle organisation
Sma-1	SPTBN5	Normal
Unc-112	FERMT1	Hypercontracted
Itr-1	ITPR1	Normal

Table S1 : List of the genes tested in the RNAi screen

Figure	Genotype	p-value
Fig1H	wild type n_embryos=7, n_waves=14	intensity cells-1/4/5 vs cells-2/3 = 0.7881 (ns);
	wild type n_embryos=14, n_waves=14	delay cells-1/4/5 vs cells-2/3 = 5.0178e-05 (***)
Fig2D	cell-2/3, (n=12 embryos) versus outside(n=12 embryos); anterior cells(n=7 embryos); tails cells(n=12 embryons)	P values, ***, p<0,0001.
Fig2E	cell-2/3, (n=8 embryos) versus outside(n=12 embryos)	Pvalue=0,0298,*,p<0,05
Fig3I	*inx-18(ok2454) n_embryos=6; n_waves=14*	Intensity: p-value cell(145) vs cell(23) = 1.1341e-05 (***)
	inx-18(ok2454) n_embryos=6; nwaves=14	delay: p-value cell(145) vs cell(23) = 0.1537 ns
	inx-15(syb5414) ,n_embryos=6; n_waves=14	Intensity: p-value cell(145) vs cell(23) = 7.5729e-09 (***)
	inx-15(syb5414) ,n_embryos=6; n_waves=14	delay: p-value cell(145) vs cell(23) = 0.6834 (ns)
Fig3K	wild type vs *inx15(syb5414); Pelt-2*::INX-15::mCherry	pvalues 0,0222,*
	*inx15(syb5414)*vs *inx15(syb5414);Pelt-2*::INX-15::mCherry	pvalues <0,0001
Fig 4D	*deg-1(u506)* embryos=8; n_waves=13	Intensity: p-value cell(145) vs cell(23) = 0.8544 (ns)
		delay: p-value cell(145) vs cell(23) = 0.4576 (ns)
	unc-105(n506) n_embryos=8; n_waves=10	Intensity: p-value cell(145) vs cell(23) = 0.4429 (ns
		delay: p-value cell(145) vs cell(23) = 0.4225 (ns)
FigS1F	*wt vs inx15(syb5414)*	pvalue= 0.224266 (ns)
	wt vs inx18(ok2454)	pvalue= 0.0310794(*)
	wt vs unc-105(n506)	pvalue= 0.311101 (ns)
FigS1E	*wt vs inx15(syb5414)*	pvalue= 0.88324
	wt vs inx18(ok2454)	pvalue= 0.026125 (*)
	wt vs unc-105(n506)	pvalue= 0.0245531 (*)

	wt vs deg-1(u506)	pvalue= 0.504298
FigS2E	p-values: wt(n_embryos=7, n_waves=14) vs *inx15(syb5414) ; inx18(ok2454)* (*n_embryos = 4* *n_waves = 11)*	cell1: 0.149607 cell2: 0.178118 cell 3: 0.0246736 cell 4: 0.049957 cell 5: 0.122759
	p-values: i *inx15(syb5414)*m vs vs *inx15(syb5414) ;, inx18(ok2454)*	cell 1: 0.0280161 cell 2: 0.421487 cell 3: 0.207633 cell 4 :0.165509 cell 5 :0.250067
	p-values: *inx18(ok2454)* vs *inx15(syb5414) ; inx18(ok2454)*	cell 1: 0.469476 cell 2: 0.378196 cell 3: 0.199428 cell 4: 0.182065 cell 5 :0.10281
FigS2F	p-values: wt(n_embryos=7, n_waves=14) vs *inx15(syb5414) ; inx18(ok2454)* (*n_embryos = 4* *n_waves = 11)*	cell 1: 7.07584e-06 cell 2: 1.45199e-05 cell 3: 4.48837e-06 cell 4: 2.59175e-06 cell 5: 0.000953831
	p-values: i *inx15(syb5414)*m vs vs *inx15(syb5414) ;, inx18(ok2454)*	cell 1: 0.0917769 cell 2: 0.00341699 cell 3: 0.00816725 cell 4 :0.0722023 cell 5 :0.483271
	p-values: *inx18(ok2454)* vs *inx15(syb5414) ; inx18(ok2454)*	cell1: 0.296586 cell 2: 0.207756 cell 3: 0.0419328 cell 4: 0.0583314 cell 5: 0.0456577

Table S2 : P values

ML2143	*(mcIs75[myo-3p::gfp::PH ; stIs10088[hlhp::his-24::mCherry; unc-119(+)]).*
ML2940	*inx-15(syb5414) I*
RB1896	*inx-18 (ok2454) IV*
HBR4	*goeIs3[pmyo-3::GCamP3.35::unc-54–3'utr, unc-119(+)] V*
N2	*Bristol*
ML2946	inx-18 (ok2454) IV ; goeIs3[pmyo-3::GCamP3.35::unc-54–3'utr, unc-119(+)]V
ML2935	mcIs1018(deg-1 ::GFP(syb5346))X
TU1366	deg-1 (u506) X
ML2944	*deg-1 (u506) X;goeIs3[pmyo-3::GCamP3.35::unc-54–3'utr, unc-119(+)] V*
CZ22703	Pmyo-3-PH-miniSOG/Pmyo-3-mCherry (juEx6916)
ZW295	*inx15p::INX15;::GFP*
ML2936	mcEx1017pelt-2::inx-15::mcherry::unc-54–3'utr
ML2943	*unc-105(n506) II,goeIs3[pmyo-3::GCamP3.35::unc-54–3'utr, unc-119(+)] V*
MT1098	unc-105(n506) II.
ML2935	Deg-1::GFP PHX4251 deg-1(syb4251),deg1::GFP
ML2934	Unc-105::GFP PHX4276 unc-105(syb4276)
OH4887	Inx18p::GFP
ML2938	*mcIs75[myo-3p::gfp::PH ,mcEx1017pelt-2::inx-15::mcherry::unc-54–3'utr*
ML2950	mcEx677[myo-3p::mCherry],unc-105(syb4276)
ML2947	mcIs1018(deg-1 ::GFP(syb5346) , mcEx677[myo-3p::mCherry]

ML2936	*mcEx1017pelt-2::inx-15::mcherry::unc-54–3'utr*
ML2946	*inx-15(syb5414) I ,inx-18 (ok2454) IV*

Tables S3 : strains used in this study